

## BIOSENSORS

# Wireless sensors for continuous, multimodal measurements at the skin interface with lower limb prostheses

Jean Won Kwak<sup>1,2,\*</sup>, Mengdi Han<sup>1\*</sup>, Zhaoqian Xie<sup>3</sup>, Ha Uk Chung<sup>4</sup>, Jong Yoon Lee<sup>4</sup>, Raudel Avila<sup>2</sup>, Jessica Yohay<sup>5</sup>, Xuexian Chen<sup>6</sup>, Cunman Liang<sup>7</sup>, Manish Patel<sup>8</sup>, Inhwa Jung<sup>9</sup>, Jongwon Kim<sup>9,10</sup>, Myeong Namkoong<sup>1,11</sup>, Kyeongha Kwon<sup>1</sup>, Xu Guo<sup>3</sup>, Christopher Ogle<sup>4</sup>, Dominic Grande<sup>4</sup>, Dennis Ryu<sup>4</sup>, Dong Hyun Kim<sup>4</sup>, Surabhi Madhvapathy<sup>1,12</sup>, Claire Liu<sup>1,13</sup>, Da Som Yang<sup>1</sup>, Yoonseok Park<sup>1</sup>, Ryan Caldwell<sup>5,14</sup>, Anthony Banks<sup>1</sup>, Shuai Xu<sup>1,4,15</sup>, Yonggang Huang<sup>2,12,16</sup>, Stefania Fatone<sup>5</sup>, John A. Rogers<sup>1,2,12,13†</sup>

Copyright © 2020  
The Authors, some  
rights reserved;  
exclusive licensee  
American Association  
for the Advancement  
of Science. No claim  
to original U.S.  
Government Works

Precise form-fitting of prosthetic sockets is important for the comfort and well-being of persons with limb amputations. Capabilities for continuous monitoring of pressure and temperature at the skin-prosthesis interface can be valuable in the fitting process and in monitoring for the development of dangerous regions of increased pressure and temperature as limb volume changes during daily activities. Conventional pressure transducers and temperature sensors cannot provide comfortable, irritation-free measurements because of their relatively rigid construction and requirements for wired interfaces to external data acquisition hardware. Here, we introduce a millimeter-scale pressure sensor that adopts a soft, three-dimensional design that integrates into a thin, flexible battery-free, wireless platform with a built-in temperature sensor to allow operation in a noninvasive, imperceptible fashion directly at the skin-prosthesis interface. The sensor system mounts on the surface of the skin of the residual limb, in single or multiple locations of interest. A wireless reader module attached to the outside of the prosthetic socket wirelessly provides power to the sensor and wirelessly receives data from it, for continuous long-range transmission to a standard consumer electronic device such as a smartphone or tablet computer. Characterization of both the sensor and the system, together with theoretical analysis of the key responses, illustrates linear, accurate responses and the ability to address the entire range of relevant pressures and to capture skin temperature accurately, both in a continuous mode. Clinical application in two prosthesis users demonstrates the functionality and feasibility of this soft, wireless system.

## INTRODUCTION

About 2 million people live with limb prostheses in the United States alone (1). A proper fit of the prosthetic socket to the residual limb is critically important to the quality of life of persons with an amputation. Ill-fitting sockets lead to friction and shear stresses between the inner surface of the socket and the skin due to pistoning (vertical displacement) and bell-clapping (sagittal plane rotation) of the limb

within the socket. The result can lead to extreme discomfort during walking for individuals with lower limb amputation. On the other hand, high pressures may cause ulcers due to excessive load bearing on the skin and underlying bony anatomy (2). Strategies to address these interface issues focus on evaluating skin responses using loading patterns representative of those associated with the prosthesis (3) and three-dimensional (3D) modeling of the fit of the prosthetic socket (4). Most of these techniques could benefit from accurate, minimally invasive, continuous measurements of pressure and temperature at the interface between the skin of the residual limb and the inner surface of the socket as real-time feedback on the nature of the fit, not just during the design process but extending to daily use. These two parameters are critically important because excessive values can lead directly to discomfort and, potentially, tissue breakdown (5), especially for people with vascular and sensory impairments, where extreme cases can lead to re-amputation (6, 7).

Current systems for pressure and temperature monitoring in this context involve sensors that do not conform well to the residual limb inside the socket and require hardwired connections to external data acquisition electronics. The rigid, bulky form factor and wired interfaces of such systems can induce damage both to the skin (8) and to the devices; these systems also limit freedom in mobility. The pressure sensors in these and other cases rely on mechanisms that range from piezoresistive (9–15) and capacitive effects (15–17) that create passive changes to piezoelectric (18, 19) and triboelectric (20, 21) mechanisms that generate active electrical signals. Disadvantages

<sup>1</sup>Querrey Simpson Institute for Bioelectronics, Northwestern University, Chicago, IL 60611, USA. <sup>2</sup>Department of Mechanical Engineering, Northwestern University, Evanston, IL 60208, USA. <sup>3</sup>State Key Laboratory of Structural Analysis for Industrial Equipment, Department of Engineering Mechanics, International Research Center for Computational Mechanics, Dalian University of Technology, Dalian 116023, China. <sup>4</sup>Sibel Inc., Evanston, IL 60208, USA. <sup>5</sup>Prosthetics-Orthotics Center, Northwestern University, Chicago, IL 60611, USA. <sup>6</sup>Academy for Advanced Interdisciplinary Studies, Peking University, Beijing, China. <sup>7</sup>Key Laboratory of Mechanism Theory and Equipment Design of Ministry of Education, School of Mechanical Engineering, Tianjin University, Tianjin, China. <sup>8</sup>University of Illinois College of Medicine at Chicago, Chicago, IL 60612, USA. <sup>9</sup>Department of Mechanical Engineering, Kyung Hee University, Yongin 17104, South Korea. <sup>10</sup>Photo-Electronic Hybrids Research Center, Korea Institute of Science and Technology (KIST), Seoul 136-791, South Korea. <sup>11</sup>Department of Biomedical Engineering, Texas A&M University, College Station, TX 77843, USA. <sup>12</sup>Department of Materials Science and Engineering, Northwestern University, Evanston, IL 60208, USA. <sup>13</sup>Department of Biomedical Engineering, Northwestern University, Evanston, IL 60208, USA. <sup>14</sup>Scheck & Siress Prosthetics and Orthotics, Schaumburg, IL 60173, USA. <sup>15</sup>Department of Dermatology, Feinberg School of Medicine, Northwestern University, Chicago, IL 60611, USA. <sup>16</sup>Department of Civil and Environmental Engineering, Northwestern University, Evanston, IL 60208, USA.

\*These authors contributed equally to this work.

†Corresponding author. Email: jrogers@northwestern.edu

include some combination of (i) operating pressure ranges (usually <100 kPa) that do not fully span those relevant to the socket-skin interface (up to 350 kPa) (12, 22–24); (ii) undesired hysteresis, drift, and nonlinearity over the full pressure range, particularly for those that rely on piezoresistive effects in soft composite materials (13, 25–27); and (iii) parasitic noise due to physical motions, prevalent in capacitive and triboelectric sensors. Although commercial flexible pressure sensors for general applications support capabilities in pressure measurements, the operating ranges are not well matched to requirements for prostheses. In addition, their relatively large sizes and rigid packages lead to discomfort on the skin inside tight-fitting sockets (12, 13). Furthermore, the physiological effects on the skin typically result not only from the effects of pressure but also from elevated temperature, accelerating negative effects on residual limb tissues. Increase in temperature causes a warm and moist environment inside the socket, makes the residual limb susceptible to bacterial infection, and potentially leads to skin breakdown (5). Measurements of pressure alone, therefore, are insufficient in conditions such as a constant small load.

Here, we report a solution to these challenges that relies on a platform for wireless, continuous monitoring of both pressure and temperature (i.e., multimodal) at multiple, critical locations (i.e., multinodal) across the socket-skin interface. The system involves a soft, thin, wireless, battery-free sensor that attaches directly to the skin inside the socket, a paired wireless module that mounts on the outside surface of the socket to wirelessly power and communicate with the sensor, and a separate portable electronic device (e.g., smartphone or tablet computer) that wirelessly receives data and displays the results in real time. This setup eliminates the need for bulky, rigid components (e.g., batteries, conventional electronics, and standard sensors) inside the socket, and it also supports continuous, long-range wireless communication to standard consumer electronics. Multiple conformable sensors placed at points of interest across the residual limb provide additional monitoring capabilities and associated insights into limb health and prosthetic fit. Application in the prosthetic sockets of two persons with transtibial and transfemoral amputation illustrate the potential for practical use of this multimodal, multinodal system.

## RESULTS

### Overall system and device configurations

The wireless, multimodal monitoring platform introduced here continuously transmits quantitative measurements of pressure and temperature from locations inside a prosthetic socket, directly at the interface with the skin of the residual limb. Figure 1 (A and B) presents schematic illustrations of the system, as implemented on a lower limb. Here, multiple battery-free sensors of pressure and temperature located at different positions of interest provide monitoring via wireless links based on combined near-field communication (NFC) and Bluetooth low energy (BLE) protocols. Specifically, each sensor pairs with a corresponding NFC/BLE module mounted on the outside surface of the prosthetic socket that provides data communication and power transfer via NFC (Fig. 1B). Batteries on this module support wireless power delivery to the battery-free device inside the socket through magnetic inductive coupling and enable data communication through this same NFC link. Furthermore, the module also allows wireless transmission of data to remote electronic devices such as tablet computers and smartphones via BLE. This dual wireless design (i) eliminates the bulk, size, weight, and health risks as-

sociated with batteries at the skin interface and (ii) allows complete freedom of motion for the prosthesis user with minimal restrictions because of the long-range capabilities of the BLE communication strategy and its compatibility with small, handheld devices such as smartphones. This latter feature represents a major advantage over purely NFC-based devices previously reported for monitoring pressure at the interface between the skin and bedding materials for patients at risk of developing bed sores (28).

A complete system of this type was applied to a person with transfemoral (above-knee) amputation walking on a treadmill, with wireless sensors and NFC/BLE modules attached to the skin and to the outside of the prosthetic socket, respectively (Fig. 1C). The module incorporates a battery pack (5.3 cm × 6 cm × 1.5 cm, with two AAA cells, 38 g) and uses a hook and loop (Velcro) fastener for mounting on the socket (Fig. 1D). The pressure/temperature sensors adopt thin, lightweight, mechanically compliant forms and wireless, battery-free operation to minimize the potential for mechanically induced irritation or injury to the residual limb. Each device has dimensions of 3 cm × 1.8 cm × 0.2 cm, a mass of 1.3 g, and a bending stiffness of 4.9 N/mm<sup>2</sup> (Fig. 1E), with the ability to bend to radii as small as 13 mm without damage to the components or constituent materials (strains induced by bending < 0.3%; fig. S1). For the two individuals evaluated, this thin, flexible design eliminated any sensation of the presence of the device when attached on the skin underneath a gel liner and prosthetic socket.

The system platform involves three main subsystems: (i) a wireless, battery-free device (sensor) for transducing pressure and temperature data into digital signals for transmission by NFC; (ii) a host module for wirelessly powering the sensor and receiving the pressure/temperature data, both via NFC, and then transmitting them to an external unit via BLE; and (iii) portable electronic device (e.g., a smartphone or tablet) for receiving the data by BLE to allow real-time display on a graphical user interface (GUI) (Fig. 1F). This overall design provides a soft interface with the residual limb to eliminate irritation, discomfort, and pain; avoids the need for batteries within the socket; and enables wireless, continuous, and multimodal monitoring at multiple anatomic locations simultaneously, with a communication range of more than 10 m. The advantages of such devices over previously demonstrated skin-interfaced pressure/temperature sensors (28) are in their high-fidelity, high-speed, accurate, and hysteresis-free responses to pressure and temperature; their soft, thin form factors and wireless operation; and their combined use of NFC and BLE protocols for wireless, battery-free sensing inside the socket and long-range operation.

### Design and characterization of the 3D pressure sensor

A key component of the system is the soft, thin pressure sensor, configured to respond via changes in resistance. This design avoids adverse parasitic effects associated with capacitive devices and complex materials and pressure responses that characterize piezoelectric and triboelectric alternatives (16–21). The layout involves metal strain gauges in a 3D framework to allow for precise, hysteresis-free measurements of pressure normal to the surface of the device. The assembly process exploits a compressive buckling technique that transforms a lithographically defined trilayer of polyimide (PI)/gold (Au)/PI (4/0.1/6 μm in thickness) as a planar, 2D precursor into a corresponding 3D structure (1.95 mm × 1.95 mm in lateral dimension, ~0.5 mm in height; Fig. 2, A to D, and fig. S2). The 3D geometry converts pressures into bending deformations, thereby inducing corresponding

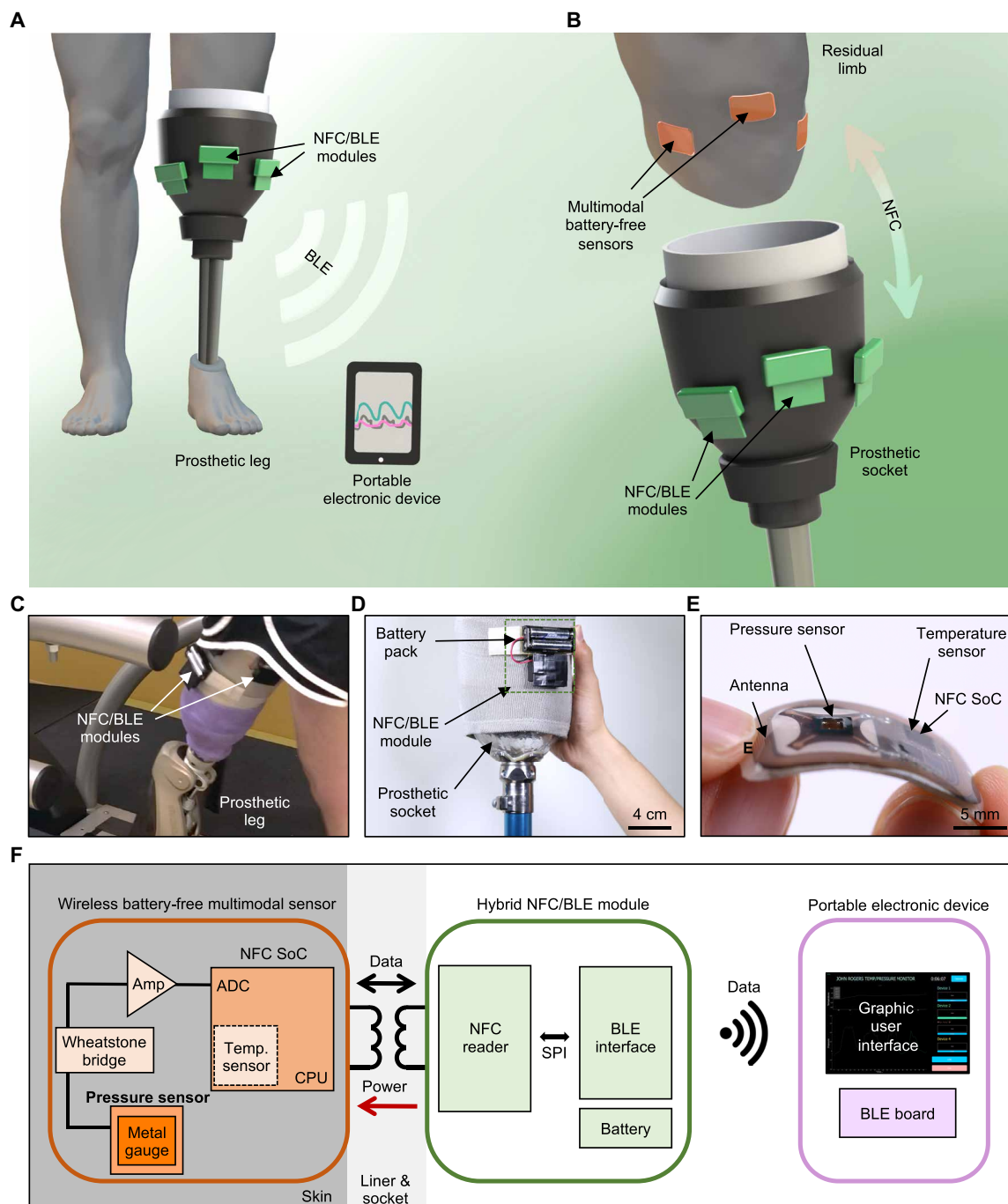


**Fig. 1. Schematic illustrations, optical images, and overview of a wireless multimodal sensing system for measurements at the interface between a residual limb and a prosthesis.** (A) Schematic illustration of the overall system. (B) Illustration of wireless, battery-free multimodal sensors on a residual limb and near-field communication (NFC)/Bluetooth low energy (BLE) modules on the outer surface of a prosthetic socket. (C) Picture of NFC/BLE modules on a socket worn by a person with amputation. (D) Picture of an NFC/BLE module attached to a socket. (E) Optical image of a multimodal sensor highlighting its flexible and thin form factor. (F) Functional block diagram showing three parts of the system: wireless, battery-free multimodal sensors; NFC/BLE module; and portable electronic device with GUI. SPI, Serial Peripheral Interface.

changes in the resistances of the strain gauges (fig. S3). In the examples here, the 2D precursor adopts a cross-shaped design, with four strain gauges (Au; 100 nm in thickness, 4- $\mu$ m trace widths in serpentine layouts) positioned along the arms of the crosses at locations optimized through finite element analysis (FEA) to maximize the sensitivity (Fig. 2, A and B, and fig. S4). Two adjacent strain gauges elec-

trically connected together increase the initial resistance (~300 ohms) and, therefore, the magnitude of the change in resistance for a given pressure. FEA results show the strain distributions in the Au during the transformation that converts the planar cross structure into a 3D table-type geometry (Fig. 2, see the “Finite element analysis (FEA)” section in Supplementary Materials and Methods). Here, openings

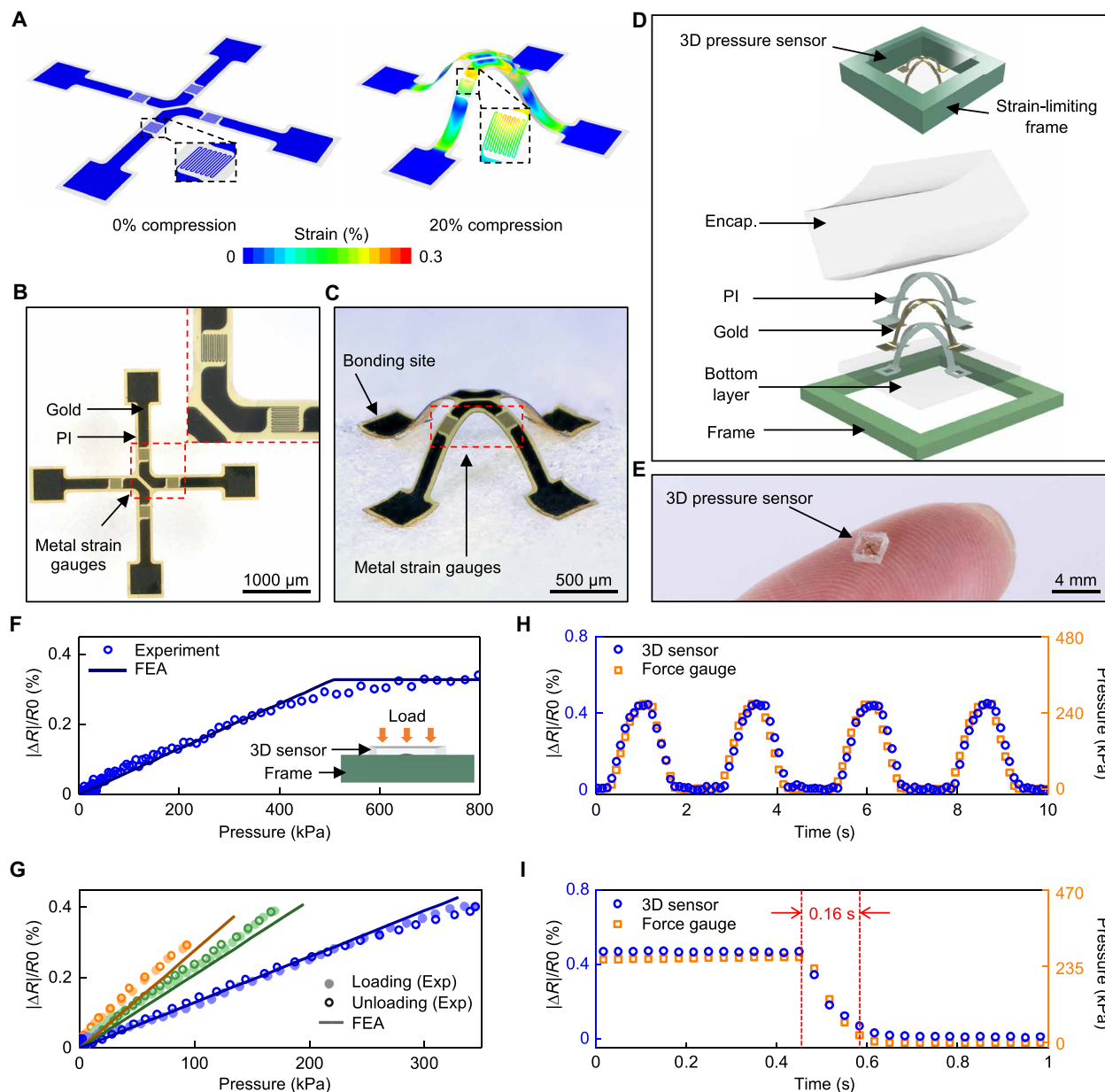


**Fig. 2. Design features and performance characteristics of 3D millimeter-scale, soft pressure sensors.** (A) Simulation results for the distribution of strain in a 2D precursor before (0% compression) and after (20% compression) transformation into a 3D shape for pressure sensing. (B) Optical image of the precursor, showing patterned thin metal traces as strain gauges. The area enclosed in the red dashed line is shown at higher magnitude in the right inset. (C) Image of the 3D mesostructure formed by compressive buckling. (D) Schematic illustration (top) and exploded view diagram (bottom) of a sensor with an encapsulation (Encap.) layer and a strain-limiting frame. (E) Picture of a pressure sensor on the tip of an index finger. (F) Fractional change in resistance ( $\Delta R/R_0$  (%)) of a sensor with a strain-limiting frame as a function of applied pressure. (G) Responses of three different sensors to pressure loading and unloading. Orange: encapsulation with modulus of 2 MPa; assembly with 20% pre-strain. Green: modulus of 2.6 MPa; prestrain of 20%. Blue: modulus of 2.6 MPa; prestrain of 15%. (H) Fractional change of resistance of a sensor under four cycles of loading/unloading compared to measurements using a force gauge. (I) Fractional change of resistance of a sensor during unloading of external pressure using a linear motion stage moving at a speed of 20 mm/s, compared to measurements using a force gauge.

(0.2 mm  $\times$  0.2 mm in lateral dimension) in the bottom PI layer leave exposed Au pads at the four bonding sites to allow for soldered electrical connections to external circuits (C400 Multicore, Loctite) (Fig. 2, B and C, 2D precursor and 3D structure, respectively).

Integration of the 3D structures with other components ensures controlled responses under normal pressures. Figure 2D illustrates a sensor that includes an encapsulation layer to provide mechanical pro-

tection and an elastic restoring force. A rigid frame around the perimeter limits the maximum extent of deformation, to avoid damage to the sensor under excessive pressures. The encapsulation consists of a silicone elastomer with dimensions of 2.4 mm  $\times$  2.4 mm  $\times$  ~0.8 mm ( $L \times W \times H$ ; Fig. 2E) and modulus of between 2 and 2.6 MPa formed by casting and curing a liquid polymer around the 3D structure in a mold that determines the overall geometry. The elastic properties of



this material define an operating range for pressures of several hundreds of kilopascals, matched to requirements for the application presented here. The frame consists of a machined printed circuit board (PCB) material (FR-4, 20 GPa modulus,  $\sim 0.68$  mm thickness,  $2.72 \text{ mm} \times 2.72 \text{ mm}$  inner lateral dimensions, and  $3.5 \text{ mm} \times 3.5 \text{ mm}$  outer lateral dimensions) with a height slightly smaller (difference in height:  $\sim 0.12$  mm) than that of the encapsulation material, to limit the overall compressive strains of the silicone encapsulation ( $< 8\%$ ) and the metal gauge ( $< 0.3\%$ ). The stress-strain curves of the silicone exhibit high linearity and low hysteresis in this range (29). Results of FEA indicate that the strain gauges also operate in an elastic range ( $< 0.3\%$ ), well below thresholds for plastic deformation (fig. S5).

The essential properties of the pressure sensor are high linearity, low hysteresis, long-term stability, fast response time, and an operating range that can be tailored to match requirements and mounting locations. The changes in resistance can be converted to pressures using a calibration process. Here, a digital multimeter (NI-USB 4065 Digital Multimeter) synchronized to a force gauge and a motorized test stand (M5-2 and ESM303, Mark-10; fig. S6, see the “Characterization of the pressure and temperature sensors” section in Supplementary Materials and Methods) yielded data to define the calibration. The measured resistance is a linear function of pressure, up to pressures ( $\sim 500$  kPa) that lead to strains limited by the frame (Fig. 2F).

The pressure sensitivity and the operating range can be tuned by adjusting the modulus of the encapsulation material or the prestrain in the compressive buckling process (Fig. 2G). For a prestrain of 20%, a sensor encapsulated with a low-modulus silicone (2 MPa, curve in orange) exhibits a higher sensitivity to pressure ( $3.1 \times 10^{-5} \text{ kPa}^{-1}$ ) and lower linear response range (from 0 to  $\sim 100$  kPa) compared to those of an otherwise similar sensor encapsulated with a slightly higher modulus silicone (2.7 MPa, curve in green, sensitivity of  $2.2 \times 10^{-5} \text{ kPa}^{-1}$  and linear range of 0 to  $\sim 180$  kPa), as might be expected intuitively.

For the same encapsulation material (silicone, modulus of 2.7 MPa), a sensor formed with a biaxial prestrain of 20% (curve in green) exhibits a higher sensitivity ( $2.2 \times 10^{-5} \text{ kPa}^{-1}$ ) and lower linear range (from 0 to  $\sim 180$  kPa) than an otherwise similar device formed with a biaxial prestrain of 15% (curve in blue, sensitivity of  $1.2 \times 10^{-5} \text{ kPa}^{-1}$ , linear range from 0 to  $\sim 400$  kPa). These trends arise from two effects. First, increasing the prestrain increases the angle of orientation of the strain gauges toward the normal direction, where they respond more directly to pressure. Second, the gauges move higher in the vertical direction as the prestrain increases. The increased height enhances deformations of the sensor in response to pressure. FEA results capture these features, consistent with experiments (Fig. 2G, lines and dots, respectively).

In all cases, the sensors show high linearity (coefficient of determination  $R^2 > 0.99$ ) and low hysteresis (hysteresis error  $< 0.02\%$ ) under loading and unloading, consistent with maximum principle strains in the silicone ( $< 8\%$ ), the metal ( $< 0.3\%$ ), and the supporting polymer ( $< 3\%$ ) that remain within ranges of linear elastic response. Such behaviors also lead to long-term stability, as supported by cyclic tests (1000 cycles; mean  $\Delta R/R$ : 0.37%, SD: 0.07%; fig. S7A). Under cyclic loading/unloading, the resistance varies with the applied pressure in the expected way and returns to its initial value at zero pressure (Fig. 2H), with negligible drift or hysteresis (correlation coefficient with the force gauge  $> 0.98$ ). Simultaneous evaluations of pressure and resistance during unloading at rates of 20 mm/s indicate that the resistance returns to its initial value with no measurable delay (limited only by the sampling rate, 30 Hz; Fig. 2I). Under a constant

static pressure, the response remains constant (correlation coefficient with the force gauge  $> 0.99$ ; fig. S7B). The soft layer underneath does not influence the sensitivity or the response time of the 3D pressure sensor (fig. S8, A and B). Under different loading rates (0.015, 0.035, and 0.05 mm/s), the response remains constant (fig. S8C). Moreover, the sensitivity is similar in a water bath ( $\sim 1$  min,  $33^\circ\text{C}$ ; sensitivities:  $3.6 \times 10^{-5} \text{ kPa}^{-1}$  for ambient air and  $3.4 \times 10^{-5} \text{ kPa}^{-1}$  for water bath, coefficient of determination  $R^2 > 0.99$  for both cases; fig. S9, A and B), demonstrating that short-term exposure to high humidity environments or sweat will not affect the performance.

In addition, the pressure sensor exhibits much lower sensitivity to shear stress ( $8.8 \times 10^{-7} \text{ kPa}^{-1}$ ; fig. S10) than to normal pressure ( $1.2 \times 10^{-5} \text{ kPa}^{-1}$ ; blue curve in Fig. 2G), and the sensitivity to normal pressure is independent of the magnitude of the shear stress (fig. S11, sensitivities of  $1.1 \times 10^{-5}$  to  $1.4 \times 10^{-5} \text{ kPa}^{-1}$ , coefficient of determination  $R^2 > 0.93$  for all cases). Although shear stress can be an important parameter for understanding the skin-prosthesis interface, this system solely focuses on normal pressure. Alternative design options to decouple normal pressure and shear stress involve two resistive elements to determine normal pressure and tangential force (14), exploiting both capacitive and resistive sensors to differentiate three separate loads (15) and integrating separate strain gauges on each leg of the 3D cross-shaped structure to decouple normal pressure and shear stress (9). The small lateral dimensions of the sensor compared to the radii of curvature of relevant parts of the residual limb [5 cm on average (30)] ensure minimal effects of bending (strain change in the Au due to bending  $< 0.002\%$ ) (Fig. 2E and fig. S1). The fabrication and assembly schemes support further miniaturization, if necessary, to meet demanding requirements. For example, sensors can be miniaturized with dimensions of  $\sim 1 \text{ mm} \times 1 \text{ mm} \times 0.3 \text{ mm}$  ( $L \times W \times H$ ) and strain gauges with feature sizes of  $2 \mu\text{m}$  (fig. S12).

### Characterization of the wireless system

Figure 3A summarizes the design features of the wireless electronics and their integration with the pressure sensor. A flexible PCB (fPCB) formed by patterning layers of copper (Cu) and PI (Cu/PI/Cu, 18/75/18  $\mu\text{m}$  in thickness, AP7164R, DuPont) serves as a substrate for the sensors and associated electronic components, along with their interconnections. A loop antenna on the fPCB ( $158.8 \text{ mm}^2$  in area) receives power by magnetic inductive coupling to the NFC/BLE module and supports wireless data transmission through this same wireless link. A mounting location on the fPCB with a planar structural element bonded on the backside (FR-4,  $\sim 0.4$  mm in thickness,  $6 \text{ mm} \times 6 \text{ mm}$  in lateral dimension) supports the pressure sensor and the strain-limiting frame. This element eliminates the influence of bending (fig. S13, sensitivities of  $1.2 \times 10^{-5}$  to  $1.4 \times 10^{-5} \text{ kPa}^{-1}$ , coefficient of determination  $R^2 > 0.97$  for all cases); low-frequency vibrations do not affect the device performance (fig. S14).

The picture in Fig. 3B shows the 3D pressure sensor integrated with various electronic components for wireless, battery-free operation. A Wheatstone bridge and an instrumentation amplifier convert and amplify the change in resistance associated with the response of the sensor into a corresponding change in voltage (fig. S15A). The amplified analog voltage signal passes through an internal analog-to-digital converter (ADC) at a sampling frequency of 10 Hz in an NFC system on a chip (SoC) before wireless transmission to the NFC/BLE module through a loop antenna tuned to 13.56 MHz (fig. S15B, see the “Sampling frequency of the device” section in Supplementary Materials and Methods). Encapsulating the entire wireless

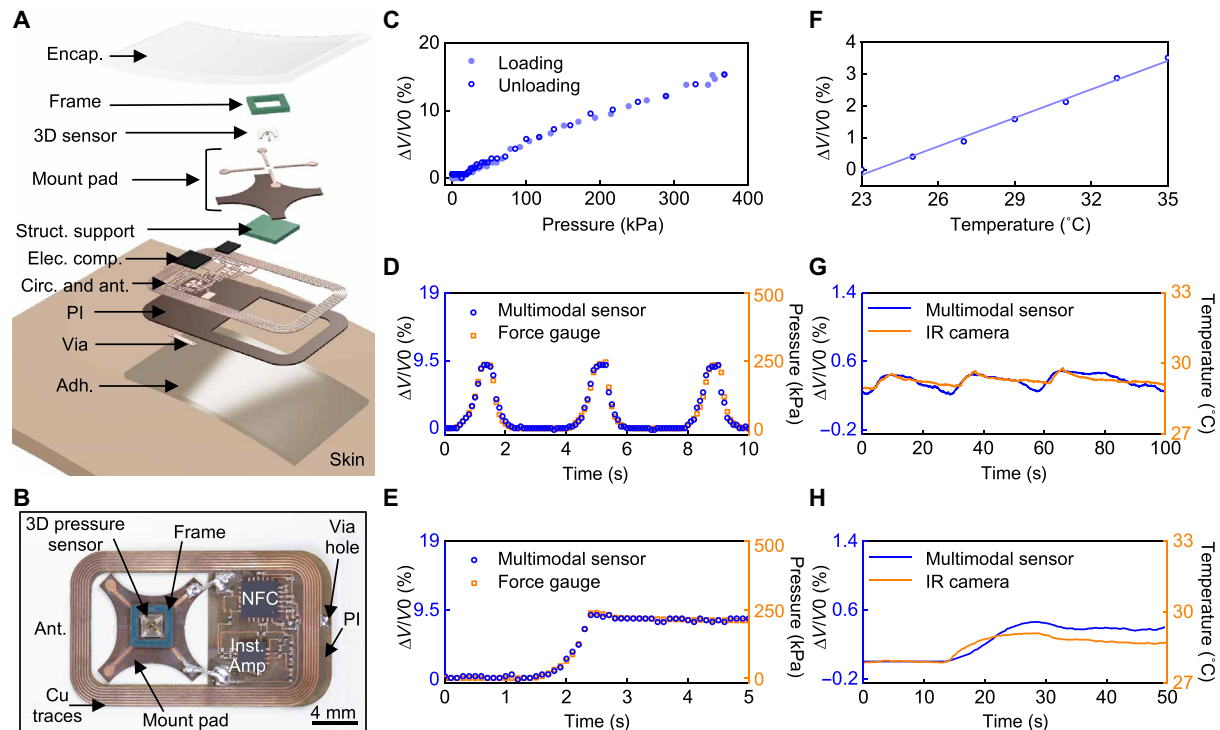


**Fig. 3. Battery-free sensors for wireless monitoring of pressure and temperature at the interface of a residual limb and a prosthesis.** (A) Exploded view schematic illustrations of the sensing device. The structural support, electronic components, circuits, antenna, and adhesive layer are abbreviated to Struct. support, Elec. comp., Circ. and ant., and Adh., respectively. (B) Picture of the device. (C) Response of the wireless sensor under pressure loading and unloading. (D) Fractional change of the analog-to-digital converter (ADC) value transmitted by the device under three cycles of loading/unloading as compared to force gauge measurements. (E) Fractional change of the ADC value under a constant load as compared to force gauge measurements. (F) Response of the wireless temperature sensor at different temperatures. (G) Fractional change of the ADC value of the wireless temperature sensor under three cycles of temperature increase and decrease as compared to infrared (IR) camera measurements. (H) Fractional change of the ADC value at a constant temperature as compared to IR camera measurements.

device (i.e., the 3D pressure sensor, electronic components, and the antenna) with a thin layer of silicone elastomer (Ecoflex 00-30, Smooth-on, 1.1 mm in thickness) mechanically protects the components and isolates them from water and biofluids (fig. S16). An adhesive (Argyle Hydrogel Adhesive Baby Tape Strips, Covidien, 1 mm in thickness) coats the bottom surface of the device to maintain contact with the skin. Characterization results indicate that the NFC communication link is effective across distances as large as ~4 cm (fig. S17A), sufficient for operation through the prosthetic socket and liner. Data transmission between the NFC/BLE module and an external electronic device (e.g., tablet with a GUI) exploits BLE protocols, with a communication range of nearly 20 m (fig. S17B). A GUI displays both pressure and temperature data in real time and allows the user to enter calibration parameters for different sensors (fig. S18).

Figure 3C presents the fractional change of the ADC values wirelessly obtained from the NFC SoC in response to different pressures, acquired through the complete wireless system. The data show a linear response ( $R^2 > 0.99$ ) with minimal hysteresis (hysteresis error  $< 0.7\%$ ) upon loading and unloading. Time-domain responses of the fractional change of the ADC value indicate good agreement with applied pressure under both cyclic (correlation coefficient with the force gauge  $> 0.99$ ; Fig. 3D) and constant (correlation coefficient with the force gauge  $> 0.99$ ; Fig. 3E) pressures. Additional demonstrations of response to dynamic and static external pressures appear in fig. S19. These results are consistent with the sensor characteristics outlined previously. In addition, the device functions properly after

10,000 cycles of compressive bending to a radius of curvature of 2 cm (fig. S20A). More severe bending (radius of curvature: ~2.5 mm) leads to damage to the connections between the sensor mounting pads and the fPCB, without damage to the pressure sensor (fig. S20B).

Wireless transmission of ADC values associated with the temperature sensor embedded in the NFC SoC yields fractional changes that correspond well to the local temperature (from 23° to 35°C; Fig. 3F, see the “Characterization of the pressure and temperature sensors” section in Supplementary Materials and Methods), as verified through comparisons to measurements obtained with an infrared (IR) camera for both time-dependent temperatures (correlation coefficient with the IR camera  $> 0.76$ ; Fig. 3G) and for constant elevated temperatures (correlation coefficient with the IR camera  $> 0.81$ ; Fig. 3H). The results indicate reliable operation in all scenarios examined. The thin adhesive layer (1 mm in thickness) enables fast response to temperature change (fig. S21A). Measurements of temperature have intrinsic value in the context of the application envisioned here, and they can also be used to eliminate the effects of temperature on the response of the pressure sensor (fig. S21B). Specifically, the pressure can be determined from the following equation, with appropriate calibration factors,

$$P = n \cdot (\text{ADC} - m \cdot (s \cdot \text{ADC}_t + c_1)) - c_2$$

where ADC is the value from the ADC channel for pressure,  $\text{ADC}_t$  is the value from the ADC channel for temperature, and  $n$ ,  $m$ ,  $s$ ,  $c_1$ ,

and  $c_2$  are constants obtained from calibration processes (fig. S21C, see the “Temperature effect on the 3D pressure sensor” section in Supplementary Materials and Methods).

### Real-time monitoring using a prosthesis simulator

Validation trials with a prosthesis simulator provide initial data on the performance and operational robustness of the system under controlled conditions. Tests involve the system mounted on the lower limbs of healthy, non-amputee volunteers ( $n = 2$ ; Fig. 4, A and B). The sensor locations include the tibial tubercle (TT), the fibular head (FH), and the medial belly of the gastrocnemius (GM) muscle, as these locations are clinically important landmarks within a prosthetic socket for an individual with lower limb amputation and represent both soft and hard (bony) areas of the residual limb (31). Each wireless device adheres directly on the skin underneath the liner, with a paired NFC/BLE module attached to the outside surface of the prosthesis simulator overlying the sensor location on the limb. The loop antennae on each wireless device and corresponding NFC/BLE module orient in a parallel orientation to maximize electromagnetic coupling. Custom fabricated by casting the volunteer’s leg, the prosthesis simulator consists of an open-ended polypropylene “socket” that encapsulates the proximal portion of the leg similar to a transtibial socket, a carbon fiber running blade (Ottobock-Sprinter) to support body weight that is partially offloaded from the anatomical foot to the proximal portion of the leg, and a thermoplastic heel cup with a hook and loop (Velcro) strap to hold the anatomical foot (fig. S22). The simulator is worn over a 6-mm gel liner (WillowWood Alpha) and held onto the limb using two knee sleeves (one proximally and one distally) and vacuum pump (WillowWood LimbLogic). The distance between the surface of the skin and the outer surface of the socket is ~1.5 cm, well within the communication range (4 cm) for the NFC power and data link.

Figure 4 (C and D) shows continuous recordings of pressure at these three locations for representative cases during sitting and standing, respectively. The wireless devices captured static pressures in different positions and distinguished variations in pressure between these two postures. Specifically, pressures at the TT and GM showed higher values (TT: mean of ~186 kPa and SD of ~7 kPa; GM: mean of ~115 kPa and SD of ~7 kPa) in the sitting condition, compared to those in the standing condition (TT: mean of ~96 kPa and SD of ~4 kPa; GM: mean of ~50 kPa and SD of ~4 kPa). Pressures at the FH exhibited different trends, where higher values occurred in the standing condition (mean of ~80 kPa and SD of ~9 kPa) compared to the sitting condition (mean of ~55 kPa and SD of ~11 kPa). In the sitting condition, the knee flexes and the femur glides anteriorly, becoming wider across the condyles. To accommodate for this, the socket may move anteriorly relative to the knee, placing greater pressure on the TT and GM. This may be an artifact of the non-amputee participant having a fully intact tibia and the simulated socket having less room to move. Figure 4E presents data collected during walking (0.67 m/s) on a treadmill, where peaks and periodic cycles in the data mimic the cyclical nature of walking, wherein the limb is loaded and unloaded during each gait cycle. The peak-to-peak difference in pressure on the FH during walking is ~94 kPa, on average; the corresponding values are ~76 and ~25 kPa for the TT and GM, respectively. The bony prominences (i.e., TT and FH) produced more pronounced peaks in pressure than the muscular region (i.e., GM), as might be expected.

Figure 4 (F and G) compares measurements performed with the wireless system to those obtained with a wired pressure sensor array

(Pilance, Novel, 100-Hz sampling rate, 10 to 600 kPa; fig. S23A) as a reference. In these evaluations, the wireless sensor directly overlays the GM, and the wired reference covers the entire surface on top of the sensor (fig. S23, B to D). A repetitive process of muscle contraction—similar to standing up on the toes and relaxing the calf to return to a foot flat position—produces expected changes in pressure on the GM. The pressures measured from the wireless device agreed with the values of pressure obtained from a nearby location on the reference array (Fig. 4F). Pressures from the wireless device and the reference on other locations or under other motions show only approximate correlations, likely due to two reasons. The first is the high detection threshold and low sensitivity of the reference sensor, which limits its ability to detect small changes in pressure and static pressures below 10 kPa. The second is the limited mechanical flexibility of the reference system, which likely leads to small gaps between the wireless and reference sensors (fig. S23, see the “Incompatibility of the reference sensor” section in Supplementary Materials and Methods).

Comparison tests for temperature use a wired thermocouple as the reference, located next to the NFC SoC on the GM, with a separation distance of ~3 mm (fig. S24), of a healthy adult volunteer. Figure 4H displays temperatures recorded with these two systems during sitting, standing, and walking. For sitting and standing, both temperatures were nearly equal and constant (29.2° and 29.6°C, respectively) with only small fluctuations (SDs: 0.08°C for the wireless device and 0.2°C for the wired reference). During walking, both temperatures increase linearly by comparable amounts ( $\Delta T$  of 4.1° and 3.4°C, respectively).

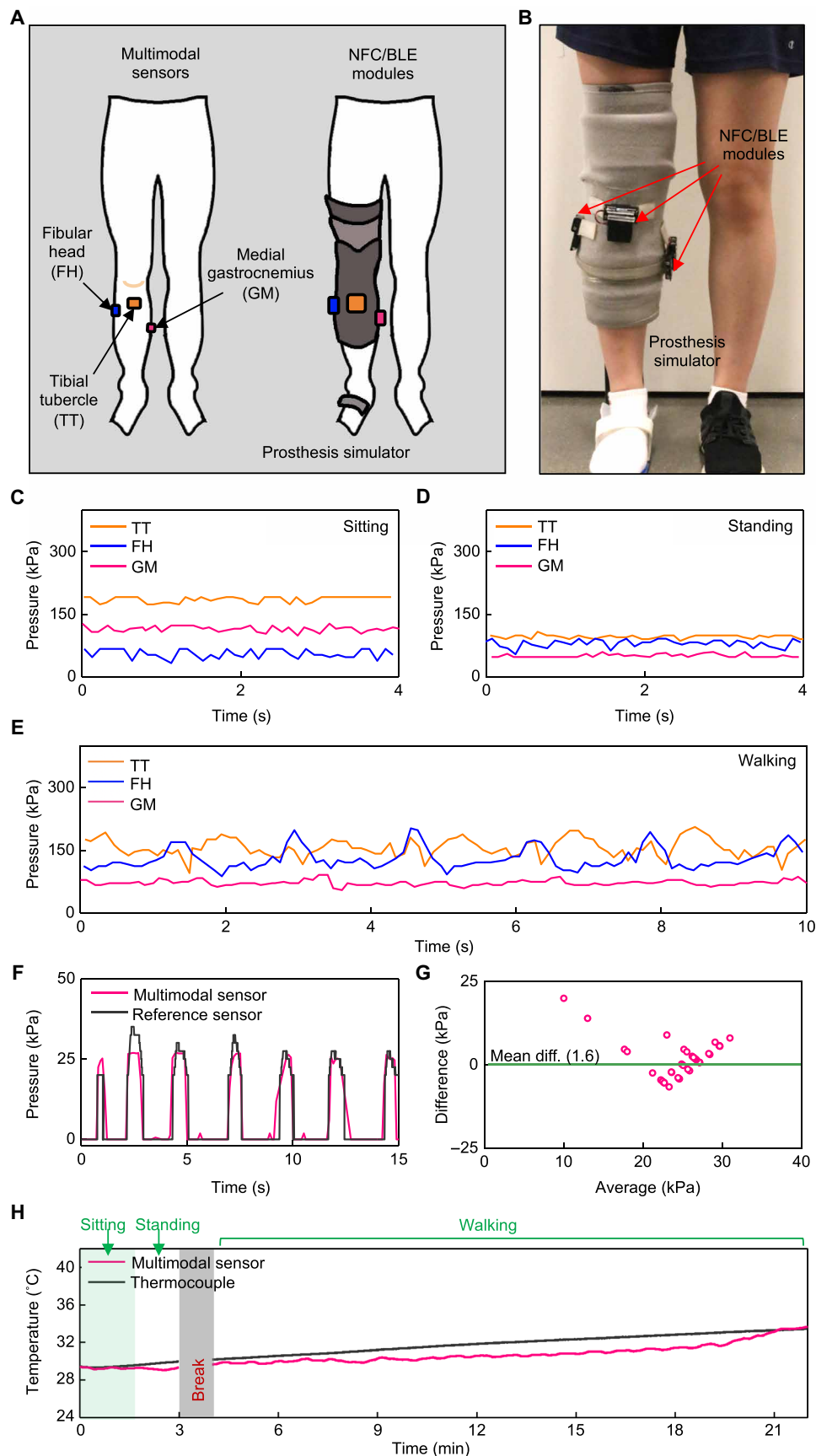
### Feasibility trials with participants with transtibial and transfemoral amputation

Measurements on individuals with transtibial (below knee; Fig. 5 and movie S1) and transfemoral (above knee; Fig. 6 and movie S2) amputations ( $n = 2$ ) demonstrate the performance and wearability of the wireless system on prosthesis users. Three mounting locations (TT, FH, and GM) on the residual limb of the individual with transtibial amputation were selected (Fig. 5A). The soft encapsulation and adhesive layer enables conformal, intimate contact to the residual limb (Fig. 5B). Mounting corresponding NFC/BLE modules on the PETG (polyethylene terephthalate glycol) socket allows real-time, continuous, wireless monitoring of pressure and temperature at the interface of the socket and skin (Fig. 5C) during sitting, standing, and walking (Fig. 5D). Pressures at the TT, FH, and GM exhibit different values due to the diverse locations and bony structures of the residual limb (22, 32). Specifically, for sitting and standing (Fig. 5, E and F), pressures at the TT were higher (mean of ~109 kPa and SD of ~12 kPa) while sitting than standing (mean of ~65 kPa and SD of ~7 kPa). Pressures at the FH and GM exhibited the opposite trends, i.e., higher while standing (FH: mean of ~122 kPa and SD of ~12 kPa; GM: mean of ~165 kPa and SD of ~5 kPa) than sitting (FH: mean of ~44 kPa and SD of ~15 kPa; GM: mean of ~64 kPa and SD of ~10 kPa). Potential influences of fluctuations for static postures include unstable standing positions, sway in the center of pressure, and motions associated with muscle contractions (33).

Figure 5 (G and H) illustrates results for pressure during walking on a treadmill (Cosmed Sport Treadmill T170) at self-selected slow (0.30 m/s) and fast (0.81 m/s) speeds. In both cases, the pressures on the TT had the smallest average values (~93 kPa in slow speed and ~85 kPa in fast speed) and average peak-to-peak differences

**Fig. 4. Wireless measurements of pressure and temperature from a non-amputee individual.**

(A) Schematic illustrations of a non-amputee participant with three sensors on the right leg and NFC/BLE modules on the outside surface of a prosthesis simulator. (B) Pictures of a prosthesis simulator with attached NFC/BLE modules. (C) Representative pressure data collected while in a sitting position. (D) Representative pressure data collected while in a standing position. (E) Representative pressure data collected while walking on a treadmill (0.67 m/s). (F) Comparison of pressure data from the wireless sensor and from a wired pressure sensor array as a reference during leg flexing (90°). (G) Bland-Altman plot for pressure data from the wireless sensor and from the wired reference during leg flexing. (H) Temperature data from the wireless sensor and from a wired thermocouple as a reference collected while sitting, standing, and walking on a treadmill (0.67 m/s). All data were collected on two individuals, separately ( $n = 2$ ).



(~63 kPa in slow speed and ~44 kPa in fast speed). During walking at slow speeds (Fig. 5G), pressure variations at the TT were less prominent than those at other locations (i.e., FH and GM) where periodic peaks were clearly visible (peak-to-peak difference: ~148 kPa for FH and ~128 kPa for GM), consistent with the cyclical nature of walking. For fast walking speeds (Fig. 5H), the pressures at all three locations (i.e., TT, FH, and GM) showed similar variations (peak-to-peak difference: ~44 kPa for TT, ~100 kPa for FH, and ~123 kPa for GM). Figure S25 (A and B) shows additional assessments of walking at self-selected normal speed (0.61 m/s) and during extended periods (2 min) while walking at faster speed (0.81 m/s). In certain circumstances, asynchronous communication between the multimodal device and NFC/BLE module led to short intervals of missing data (fig. S26, see the “Voltage drop artifacts” section in Supplementary Materials and Methods). Automated MATLAB codes eliminated these intervals from data analysis (fig. S27, see the “MATLAB codes for removing voltage drops” section in Supplementary Materials and Methods).

Continuous monitoring of temperature, simultaneously with pressure, is also possible, as demonstrated in Fig. 5I. During sitting and standing conditions, temperatures in all locations remained nearly constant ( $\Delta T < 0.4^\circ\text{C}$ , SDs  $< 0.02^\circ\text{C}$ ). During walking, the temperatures in the three



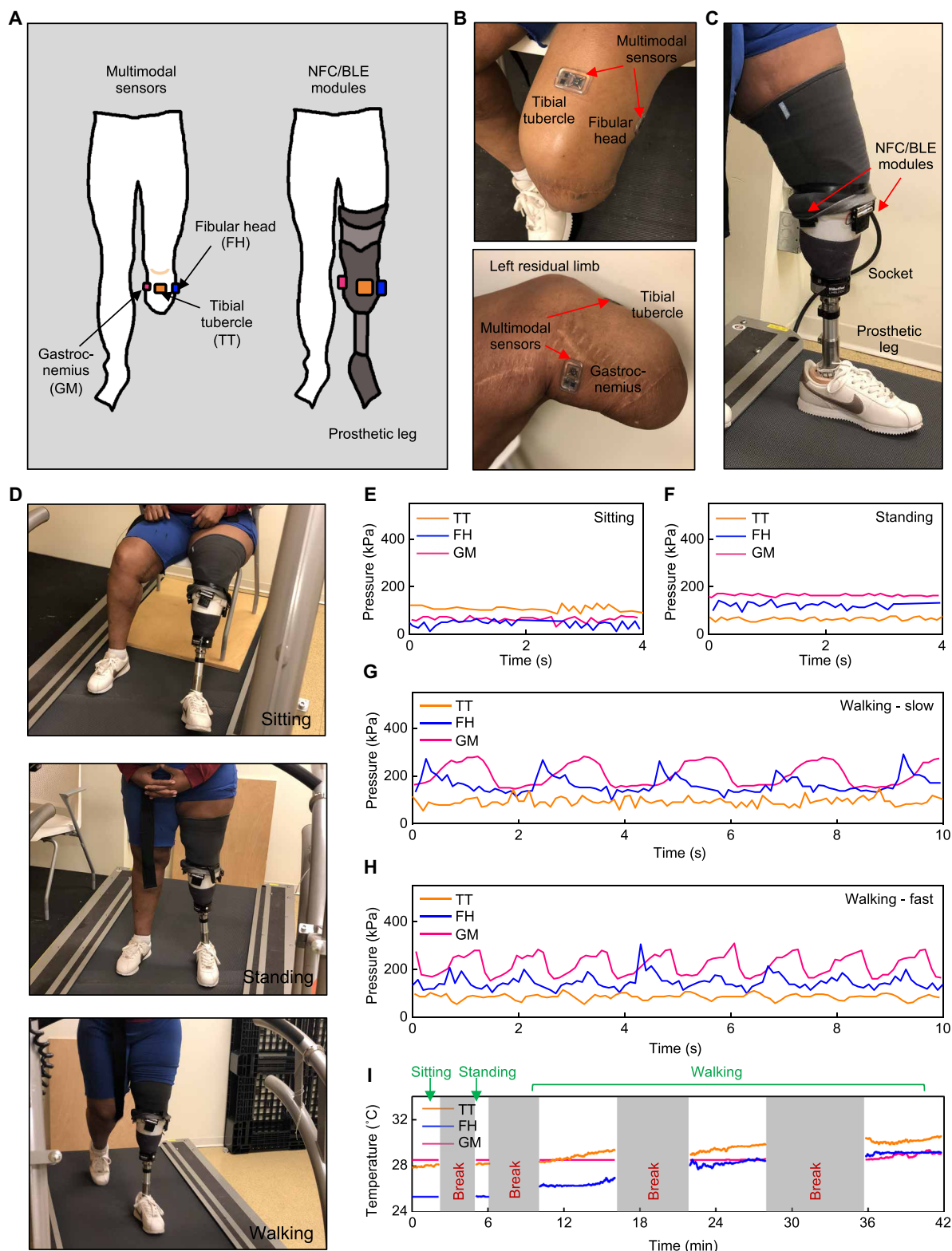


**Fig. 5. Wireless measurements of pressure and temperature from a participant with transtibial amputation.** (A) Schematic illustrations of an individual with transtibial amputation with three multimodal sensors on the residual limb and NFC/BLE modules on the prosthesis. (B) Pictures of the transtibial residual limb with wireless sensors adhered to different locations. (C) Picture of a prosthesis with attached NFC/BLE modules. (D) Pictures of the participant during three different activities. (E) Representative pressure data collected while in a sitting position. (F) Representative pressure data collected while in a standing position. (G) Representative pressure data collected while walking on a treadmill at a self-selected slow speed (0.31 m/s). (H) Representative pressure data collected while walking on a treadmill at a self-selected fast speed (0.81 m/s). (I) Temperature data collected throughout the testing protocol. All data were collected on a single participant ( $n = 1$ ).

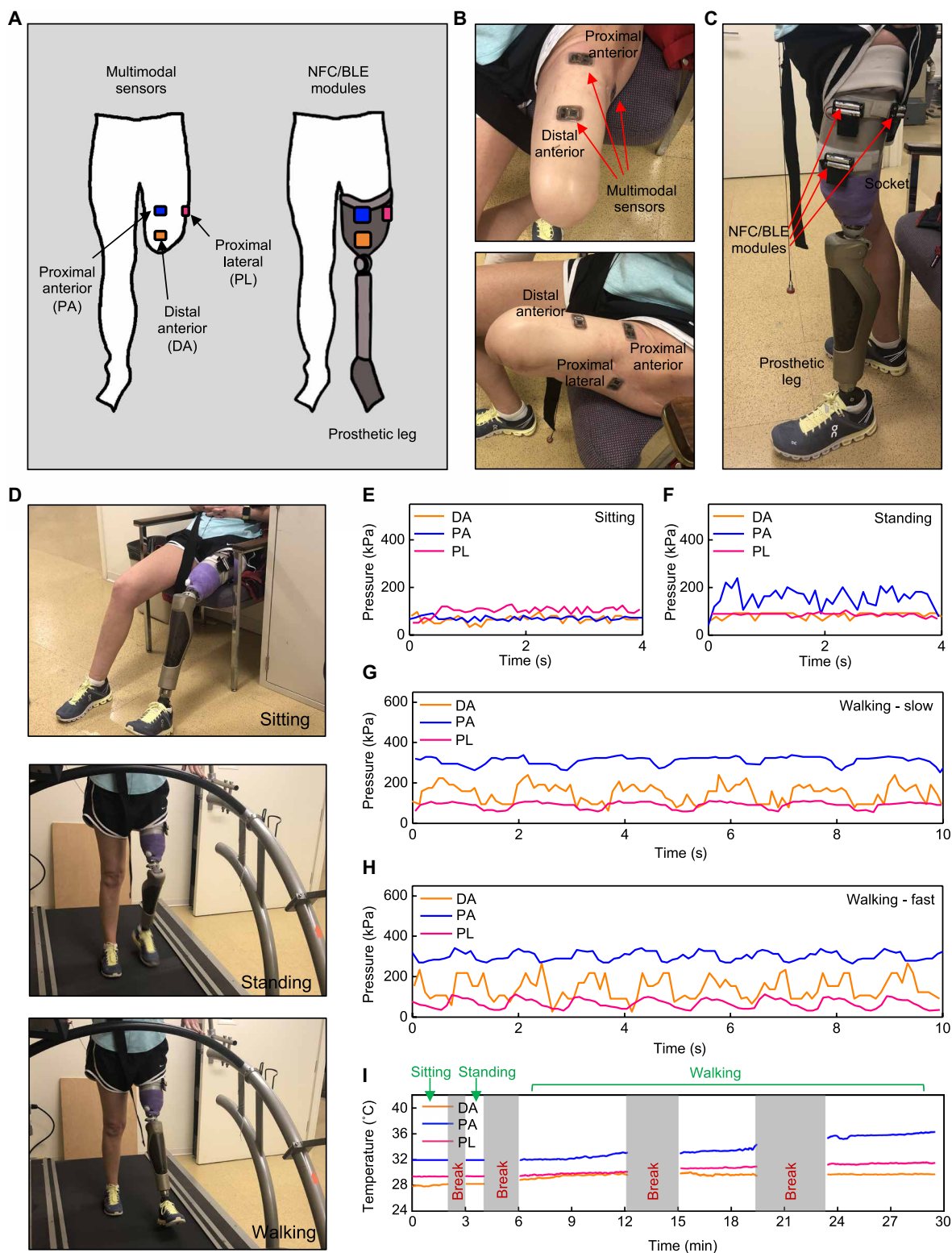


**Fig. 6. Wireless measurements of pressure and temperature from a participant with transfemoral amputation.** (A) Schematic illustrations of an individual with transfemoral amputation with three multimodal sensors on the residual limb and NFC/BLE modules on the prosthesis. (B) Pictures of the transfemoral residual limb with wireless sensors adhered to different locations. (C) Pictures of a prosthesis with attached NFC/BLE modules. (D) Pictures of the participant during three different activities. (E) Representative pressure data collected while in a sitting position. (F) Representative pressure data collected while in a standing position. (G) Representative pressure data collected while walking on a treadmill at a slow self-selected speed (0.39 m/s). (H) Representative pressure data collected while walking on a treadmill at a fast self-selected speed (0.88 m/s). (I) Temperature data collected throughout the testing protocol. All data were collected on a single participant ( $n = 1$ ).

locations increased with time, with the largest changes observed at the FH ( $\Delta T = 2.3^\circ$ ,  $2.8^\circ$ , and  $0.6^\circ\text{C}$ , on average for the TT, FH, and GM, respectively).

For persons with transfemoral amputation, the residual limb does not include the knee. The distal anterior (DA), proximal anterior (PA), and proximal lateral (PL) regions, in this case, serve as the locations for pressure and temperature monitoring (Fig. 6, A to C). The prosthesis in this case contains a prosthetic knee (OttoBock C-leg 4) connected to a PETG socket. A subject participant performed sitting, standing, and walking (Fig. 6D), and three NFC/BLE modules collected the pressures and temperatures at DA, PA, and PL regions (Fig. 6, E and F). The DA and PA showed higher pressures during the standing condition (DA: mean of  $\sim 86$  kPa and SD of  $\sim 11$  kPa; PA: mean of  $\sim 155$  kPa and SD of  $\sim 36$  kPa) than during the sitting condition (DA: mean of  $\sim 66$  kPa and SD of  $\sim 14$  kPa; PA: mean of  $\sim 67$  kPa and SD of  $\sim 18$  kPa). In comparison, PL showed smaller pressures during standing (mean of  $\sim 85$  kPa and SD of  $\sim 7$  kPa) than sitting (mean of  $\sim 102$  kPa and SD of  $\sim 17$  kPa). The results here imply that the body weight experienced on the DA and PA while standing are larger than while sitting, whereas the PL shows an opposite trend. Similar to the individual with transtibial amputation, unstable standing position with greater sway of the center of pressure and muscle contraction may have contributed to fluctuations in the pressure values.

Figure 6 (G and H) and fig. S25C highlight measurements of pressure during walking on a treadmill (Cosmed Sport Treadmill T170) at self-selected slow (0.39 m/s), normal (0.65 m/s), and fast speeds (0.88 m/s). Pressures in all three locations (i.e., DA, PA, and PL) exhibited cyclical patterns consistent with the cyclical nature of walking. Pressures on the PA were the highest ( $\sim 312$  kPa for slow speed and  $\sim 301$  kPa for fast speed), and the peak-to-peak differences in pressure were  $\sim 68$  kPa for both slow and fast speeds. The DA exhibited higher peak-to-peak differences in pressure than those at the PL (slow speed: DA:  $\sim 141$  kPa, PL:  $\sim 49$  kPa; fast speed: DA:  $\sim 165$  kPa, PL:  $\sim 69$  kPa).

Figure 6I displays results for temperature. During sitting and standing, the temperatures remained nearly constant, at  $28.1^\circ$ ,  $31.9^\circ$ , and  $29.4^\circ\text{C}$  for the DA, PA, and PL, respectively, on average (SDs  $< 0.02^\circ\text{C}$ ). During walking, the temperature at the PA exhibited larger increase ( $\Delta T$  of  $4^\circ\text{C}$ ) compared with those at the DA and PL ( $\Delta T$  of  $1^\circ$  and  $2^\circ\text{C}$ , respectively). These trends in temperature correspond with the pressure results; the increase in temperature at the PA is the highest, where the average pressure is also the largest.

## DISCUSSION

This paper introduces a wireless system capable of continuous monitoring of temperature and pressure using thin, battery-free sensors located at the interface between the gel liner and hard prosthetic socket and the soft skin of the residual limb. The resulting information, collected at multiple locations on the residual limb without mechanical perturbation or irritation of the skin surface, can yield insights not only into the initial fit of the prosthesis but also into continuous changes in fit associated with diurnal and activity-related fluctuations in residual limb volume. The capabilities rely critically on two main advances over previously reported technologies: (i) a miniaturized soft pressure sensor that adopts a 3D architecture to meet all measurement requirements, such as minimum hysteresis, absence of drift, and high linearity, and (ii) a dual wireless design that eliminates the need for battery power on the sensor platform and provides long-range communication capabilities to standard con-

sumer electronic devices. Benchtop studies, numerical simulations, evaluations on non-amputees, and initial trials on both transtibial and transfemoral prosthesis users demonstrate feasibility of all the key functional aspects as well as the practical utility of this system in continuous monitoring of pressure and temperature. The sensors and the wireless strategies have potential for uses in other medical contexts such as those in patients at risk for the development of pressure ulcers and with individuals using wearable robots for rehabilitation. Further investigations may include integration with different types of sensors like humidity or wireless communication inside sockets constructed of different types of materials.

For monitoring of skin under a prosthesis, measurements of shear stress are needed for a complete understanding of skin injuries, as shear stresses produce physical friction and resistance at the interface between skin and prosthetic socket. Replacing the NFC SoC with a BLE SoC can provide additional ADC channels, allowing for simultaneous monitoring of normal pressure, shear stress, and temperature but at the expense of increased power consumption and associated practical difficulties with operation in a battery-free mode. This study focused, instead, on normal pressure by the design of a strain-limiting frame that limits the effects of shear stress on the sensor response. Further optimization of the wireless platform and/or algorithm will enable real-time, continuous display of multimodal physiological signals and automatic detection/evaluation of prosthetic fitness. Expanding the number of human participants and increasing the range of types of amputations will enhance an understanding of mechanisms that lead to skin damage.

## MATERIALS AND METHODS

### Study design

The purpose of the study was to develop and demonstrate miniaturized, soft pressure sensors with a thin, battery-free, wireless design for use at the interface between the skin and the inner surface of a prosthesis. Investigators at the Northwestern University Prosthetics-Orthotics Center recruited participants with and without amputations to test the feasibility of these devices. Three different anatomic locations were selected depending on different levels of amputation. The process of cleaning preselected areas of the residual limb for device placements involved gentle rubbing with alcohol wipes. After placing multimodal devices at these locations, the participants donned their gel liners (and sock, if necessary) and, following a confirmation of wireless connectivity, donned their sockets over the liners. Mounting NFC/BLE modules with hook fasteners (Velcro) allowed placement on the surfaces of the sockets with corresponding loop fasteners (Velcro). Data recording began after 10 s of walking in place to ensure device stabilization. Each individual performed the following activities: 2 min of sitting at rest, 2 min of standing, and 6 min each of walking at a self-selected normal, slow, and fast speed on a treadmill (Cosmed Sport Treadmill T170). When requested, the individuals rested in between activities while wearing the devices. After data collection, the individuals doffed the prosthetic components to allow inspection of the skin of the residual limbs at the sensor locations. Details of each participant appear in table S1, and collected primary data are shown in data file S1.

### Fabrication of 3D pressure sensors

Preparation of the 2D precursors began with deposition of Cu (100 nm in thickness) via electron beam evaporation on a silicon wafer, as a sacrificial layer for a release process described subsequently.



Spin coating (1500 rpm for 60 s) and curing (250°C for 2 hours) a layer of PI (HD MicroSystems) on the Cu-coated wafer, followed by photolithography, defined a pattern of photoresist (AZ 2035, MicroChem) for a lift-off procedure. Uniform deposition of Cr/Au (10 nm/100 nm in thickness) via electron beam evaporation followed by immersion in acetone yielded patterns of Cr/Au. After spin coating another layer of PI (1000 rpm for 60 s) and depositing another layer of Cu (100 nm in thickness), photolithography defined a pattern of photoresist (AZ 5214, MicroChem) to define the outline of the cross-shaped 2D precursor. Dry etching by reactive ion (March RIE, 220 mtorr, 200 W, 25 sccm of O<sub>2</sub>, ~40 min) of PI completed the fabrication of the precursor. Wet etching of Cu (CE-100 copper etchant, Transene) undercut the sacrificial layer to release the 2D precursors from the silicon wafer and removed the Cu mask layer. Either manual or automated assembly transformed the 2D precursors into 3D structures. Manual assembly process used solder (C400 Multicore, Loctite) to fix the bonding sites of the 2D precursors to a mount pad (i.e., Cu traces and pads on a PI sheet) patterned by an ultraviolet (UV) laser system (ProtoLaser U4, LPKF). Smaller distances between the Cu pads (compared with that between the bonding sites) induced buckling of the 2D precursors. Automated mode of assembly exploited compressive buckling (34) and physical transfer of 3D structures (35) for such 2D to 3D transformations. Casting and curing a precursor to poly(dimethylsiloxane) (PDMS; Sylgard 184, Dow Corning) onto the 3D structures with a mold in FR-4 (2.4 mm × 2.4 mm × 0.8 mm in  $L \times W \times H$ ) completed the fabrication. A piece of FR-4 cut with a UV laser system (ProtoLaser U4, LPKF) produced frames to desired sizes and thicknesses, for manual placement onto the mounting position around the sensor.

### Assembly and encapsulation of pressure sensors and wireless circuits

A sheet of PI (75 μm) with annealed Cu (18 μm) on both sides served as the substrate. A UV laser system (ProtoLaser U4, LPKF) patterned and ablated the PI and Cu to yield the pads and interconnect traces for the circuit. In/Ag soldering paste (Ind. 290, Indium Corporation) connected surface-mounted electrical components, including the pressure sensor, to these traces. A thin film of an elastomer (Argyle Hydrogel Adhesive Baby Tape Strips, Covidien) served as a bottom layer of an encapsulation structure. Placing the circuit on this layer, followed by casting and curing a soft elastomer (Ecoflex 00-30, Smooth-on) on top, completed the process.

### Design of the circuit

The circuit included the sensor as part of a Wheatstone bridge to convert the change in resistance to a change in voltage, an instrumentation amplifier (fig. S15A) to amplify this voltage signal, an NFC SoC with ADC to digitize the signal at a sampling frequency of 10 Hz, an on-chip temperature sensor within the NFC SoC, surface-mounted resistors and capacitors as peripheral components, and a radio frequency (RF) loop antenna configured at 13.56 MHz for NFC protocols. A piece of fPCB served as the substrate (fig. S28). The host module on the prosthetic socket included an NFC reader (TRF79x0ATB, Texas Instruments) to provide wireless power transmission and data communication with the sensing device inside the socket, and a BLE system that transfers data obtained from the reader to a separate PC tablet with a custom GUI for data visualization and storage (fig. S29A). Each NFC reader (fig. S29B) pairs with a BLE unit to enable stable wireless power transfer and data exchange. The BLE system consisted

of a microcontroller (nRF52832, Nordic Semiconductor) to communicate and receive data, two oscillators, an antenna for the BLE radio at 2.4 GHz, an interface to the NFC reader, and a holder to accommodate two AAA batteries (fig. S29). The system can operate for 2 hours of continuously powering the NFC reader, transferring power to and receiving data from the device, and communicating through BLE to a portable electronic device.

### Statistical analysis

Data are presented as single values. Statistical analysis was not performed except for the Bland-Altman plot (Fig. 4G) because this paper contains a small number of clinical proof-of-concept trials. Linear regression analysis of measured sensor data generated calibration curves. OriginPro computed  $R^2$ , and the slope of the linear fit was used to determine calibration factors.

### SUPPLEMENTARY MATERIALS

stm.sciencemag.org/cgi/content/full/12/574/eabc4327/DC1

Materials and Methods

Fig. S1. Simulated distributions of strain in the Cu/Au layers.

Fig. S2. Schematic illustration of the process for fabricating the sensor.

Fig. S3. Cross-sectional views.

Fig. S4. 2D layout of the sensor.

Fig. S5. Simulation of distributions of changes in strain.

Fig. S6. Optical image of the measurement setup and equipment.

Fig. S7. Additional performance characteristics of the 3D pressure sensors.

Fig. S8. Additional performance characteristics of the 3D pressure sensors under various settings.

Fig. S9. Characteristics of the encapsulation layer and pressure sensor in two different thermal and humidity conditions.

Fig. S10. Response of the sensor under shear stress.

Fig. S11. Sensor performance to normal pressure under different shear stresses.

Fig. S12. Optical image of a pressure sensor.

Fig. S13. Bending insensitivity of the sensor with the structural support.

Fig. S14. Measurements that indicate an insensitivity to low-frequency vibrations.

Fig. S15. Additional information about the circuit.

Fig. S16. Images of the multimodal device operated in water.

Fig. S17. Device specifications of communication distances.

Fig. S18. Screenshot of the GUI.

Fig. S19. Responses of the wireless device under different mechanical stimuli.

Fig. S20. Device under compressive bending.

Fig. S21. Thermal characteristics of the on-chip temperature sensor and the 3D pressure sensor.

Fig. S22. Optical images of a prosthesis simulator.

Fig. S23. Optical images and additional pressure data of comparison testing.

Fig. S24. Optical images of the temperature comparison test.

Fig. S25. Additional pressure data from subjects.

Fig. S26. Wirelessly powered ADC output at different sampling rates.

Fig. S27. Postprocessing of data using MATLAB.

Fig. S28. CAD design of the NFC circuit.

Fig. S29. Hybrid NFC/BLE module.

Table S1. Summary of participants for clinical trials.

Data file S1. Primary data.

Data file S2. MATLAB code to identify the cycle.

Movie S1. Subject with transtibial amputation.

Movie S2. Subject with transfemoral amputation.

References (36–38)

View/request a protocol for this paper from [Bio-protocol](https://doi.org/10.1126/sciencemag.12574.eabc4327).

### REFERENCES AND NOTES

1. K. Ziegler-Graham, E. J. MacKenzie, P. L. Ephraim, T. G. Trivison, R. Brookmeyer, Estimating the prevalence of limb loss in the United States: 2005 to 2050. *Arch. Phys. Med. Rehabil.* **89**, 422–429 (2008).
2. S. Roy, S. S. Mathew-Steiner, C. K. Sen, in *Prosthesis* (IntechOpen, 2019).
3. J. L. Bramley, P. R. Worsley, L. E. Bostan, D. L. Bader, A. S. Dickinson, Establishing a measurement array to assess tissue tolerance during loading representative of prosthetic use. *Med. Eng. Phys.* **78**, 39–47 (2020).
4. Z. Shuxian, Z. Wanhua, L. Bingheng, 3D reconstruction of the structure of a residual limb for customising the design of a prosthetic socket. *Med. Eng. Phys.* **27**, 67–74 (2005).



5. L. E. Diment, M. S. Thompson, J. H. M. Bergmann, Comparing thermal discomfort with skin temperature response of lower-limb prosthesis users during exercise. *Clin. Biomech. (Bristol, Avon)* **69**, 148–155 (2019).
6. Y. Izumi, K. Satterfield, S. Lee, L. B. Harkless, Risk of reamputation in diabetic patients stratified by limb and level of amputation: A 10-year observation. *Diabetes Care* **29**, 566–570 (2006).
7. K. Hagberg, R. Brånemark, Consequences of non-vascular trans-femoral amputation: A survey of quality of life, prosthetic use and problems. *Prosthet. Orthot. Int.* **25**, 186–194 (2001).
8. D. L. Bader, P. R. Worsley, A. Gefen, Bioengineering considerations in the prevention of medical device-related pressure ulcers. *Clin. Biomech. (Bristol, Avon)* **67**, 70–77 (2019).
9. S. M. Won, H. Wang, B. H. Kim, K. Lee, H. Jang, K. Kwon, M. Han, K. E. Crawford, H. Li, Y. Lee, X. Yuan, S. B. Kim, Y. S. Oh, W. J. Jang, J. Y. Lee, S. Han, J. Kim, X. Wang, Z. Xie, Y. Zhang, Y. Huang, J. A. Rogers, Multimodal sensing with a three-dimensional piezoresistive structure. *ACS Nano* **13**, 10972–10979 (2019).
10. C.-L. Choong, M.-B. Shim, B.-S. Lee, S. Jeon, D.-S. Ko, T.-H. Kang, J. Bae, S. H. Lee, K.-E. Byun, J. Im, Y. J. Jeong, C. E. Park, J.-J. Park, U.-I. Chung, Highly stretchable resistive pressure sensors using a conductive elastomeric composite on a micropillar array. *Adv. Mater.* **26**, 3451–3458 (2014).
11. D. J. Lipomi, M. Vosgueritchian, B. C.-K. Tee, S. L. Hellstrom, J. A. Lee, C. H. Fox, Z. Bao, Skin-like pressure and strain sensors based on transparent elastic films of carbon nanotubes. *Nat. Nanotechnol.* **6**, 788–792 (2011).
12. L. Pelliccia, M. Schumann, M. Dudczig, M. Lamonaca, P. Klimant, G. Di Gironimo, Implementation of tactile sensors on a 3-Fingers Robotiq® adaptive gripper and visualization in VR using Arduino controller. *Procedia CIRP* **67**, 250–255 (2018).
13. A. Nag, S. C. Mukhopadhyay, Occupancy detection at smart home using real-time dynamic thresholding of flexiforce sensor. *IEEE Sens. J.* **15**, 4457–4463 (2015).
14. Y. Song, W. Huang, C. Mu, X. Chen, Q. Zhang, A. Ran, Z. Peng, R. Sun, W. Xie, Carbon nanotube-modified fabric for wearable smart electronic-skin with exclusive normal-tangential force sensing ability. *Adv. Mater. Technol.* **4**, 1800680 (2019).
15. S. Peng, S. Wu, Y. Yu, B. Xia, N. H. Lovell, C. H. Wang, Multimodal capacitive and piezoresistive sensor for simultaneous measurement of multiple forces. *ACS Appl. Mater. Interfaces* **12**, 22179–22190 (2020).
16. S.-K. Kang, R. K. J. Murphy, S.-W. Hwang, S. M. Lee, D. V. Harburg, N. A. Krueger, J. Shin, P. Gamble, H. Cheng, S. Yu, Z. Liu, J. G. McCall, M. Stephen, H. Ying, J. Kim, G. Park, R. C. Webb, C. H. Lee, S. Chung, D. S. Wie, A. D. Gujar, B. Vemulapalli, A. H. Kim, K.-M. Lee, J. Cheng, Y. Huang, S. H. Lee, P. V. Braun, W. Z. Ray, J. A. Rogers, Bioresorbable silicon electronic sensors for the brain. *Nature* **530**, 71–76 (2016).
17. S. C. B. Mannsfeld, B. C.-K. Tee, R. M. Stoltenberg, C. V. H.-H. Chen, S. Barman, B. V. O. Muir, A. N. Sokolov, C. Reese, Z. Bao, Highly sensitive flexible pressure sensors with microstructured rubber dielectric layers. *Nat. Mater.* **9**, 859–864 (2010).
18. M. Han, H. Wang, Y. Yang, C. Liang, W. Bai, Z. Yan, H. Li, Y. Xue, X. Wang, B. Akar, H. Zhao, H. Luan, J. Lim, I. Kandela, G. A. Ameer, Y. Zhang, Y. Huang, J. A. Rogers, Three-dimensional piezoelectric polymer microsystems for vibrational energy harvesting, robotic interfaces and biomedical implants. *Nat. Electron.* **2**, 26–35 (2019).
19. W. Wu, X. Wen, Z. L. Wang, Taxel-addressable matrix of vertical-nanowire piezotronic transistors for active and adaptive tactile imaging. *Science* **340**, 952–957 (2013).
20. K. Y. Lee, H.-J. Yoon, T. Jiang, X. Wen, W. Seung, S.-W. Kim, Z. L. Wang, Fully packaged self-powered triboelectric pressure sensor using hemispheres-array. *Adv. Energy Mater.* **6**, 1502566 (2016).
21. F.-R. Fan, L. Lin, G. Zhu, W. Wu, R. Zhang, Z. L. Wang, Transparent triboelectric nanogenerators and self-powered pressure sensors based on micropatterned plastic films. *Nano Lett.* **12**, 3109–3114 (2012).
22. E. A. Al-Fakih, N. A. A. Osman, F. R. M. Adikan, A. Eshraghi, P. Jahanshahi, Development and validation of fiber Bragg grating sensing pad for interface pressure measurements within prosthetic sockets. *IEEE Sens. J.* **16**, 965–974 (2015).
23. F. Jasni, N. A. Hamzaid, T. Y. Al-Nusairi, N. H. M. Yusof, H. N. Shasmin, S.-C. Ng, Feasibility of a gait phase identification tool for transfemoral amputees using piezoelectric-based in-socket sensory system. *IEEE Sens. J.* **19**, 6437–6444 (2019).
24. L. Paternò, M. Ibrahim, E. Gruppioni, A. Mencias, L. Ricotti, Sockets for limb prostheses: A review of existing technologies and open challenges. *IEEE Trans. Biomed. Eng.* **65**, 1996–2010 (2018).
25. J.-S. Kim, G.-W. Kim, Hysteresis compensation of piezoresistive carbon nanotube/polydimethylsiloxane composite-based force sensors. *Sensors (Basel)* **17**, 229 (2017).
26. S. Sundaram, P. Kellnhofer, Y. Li, J.-Y. Zhu, A. Torralba, W. Matusik, Learning the signatures of the human grasp using a scalable tactile glove. *Nature* **569**, 698–702 (2019).
27. Y. Song, H. Chen, Z. Su, X. Chen, L. Miao, J. Zhang, X. Cheng, H. Zhang, Highly compressible integrated supercapacitor–piezoresistance–sensor system with CNT-PDMS sponge for health monitoring. *Small* **13**, 1702091 (2017).
28. S. Han, J. Kim, S. M. Won, Y. Ma, D. Kang, Z. Xie, K.-T. Lee, H. U. Chung, A. Banks, S. Min, Y. Y. Heo, C. R. Davies, J. W. Lee, C.-H. Lee, B. H. Kim, K. Li, Y. Zhou, C. Wei, X. Feng, Y. Huang, J. A. Rogers, Battery-free, wireless sensors for full-body pressure and temperature mapping. *Sci. Transl. Med.* **10**, eaan4950 (2018).
29. A. Rinaldi, A. Tamburrano, M. Fortunato, M. S. Sarto, A flexible and highly sensitive pressure sensor based on a PDMS foam coated with graphene nanoplatelets. *Sensors (Basel)* **16**, 2148 (2016).
30. G. R. Fernie, P. J. Holliday, Volume fluctuations in the residual limbs of lower limb amputees. *Arch. Phys. Med. Rehabil.* **63**, 162–165 (1982).
31. S. Huang, D. P. Ferris, Muscle activation patterns during walking from transtibial amputees recorded within the residual limb-prosthetic interface. *J. Neuroeng. Rehabil.* **9**, 55 (2012).
32. E. Peuker, M. Cummings, Anatomy for the acupuncturist—Facts & fiction 3: Upper & lower extremity. *Acupunct. Med.* **21**, 112–122 (2003).
33. M. Wakasa, K. Seki, A. Fukuda, K. Sasaki, S.-i. Izumi, Muscle activity and postural control during standing of healthy adults wearing a simulated trans-femoral prosthesis. *J. Phys. Ther. Sci.* **22**, 233–238 (2010).
34. S. Xu, Z. Yan, K.-I. Jang, W. Huang, H. Fu, J. Kim, Z. Wei, M. Flavin, J. McCracken, R. Wang, A. Badea, Y. Liu, D. Xiao, G. Zhou, J. Lee, H. U. Chung, H. Cheng, W. Ren, A. Banks, X. Li, U. Paik, R. G. Nuzzo, Y. Huang, Y. Zhang, J. A. Rogers, Assembly of micro/nanomaterials into complex, three-dimensional architectures by compressive buckling. *Science* **347**, 154–159 (2015).
35. Z. Yan, M. Han, Y. Shi, A. Badea, Y. Yang, A. Kulkarni, E. Hanson, M. E. Kandel, X. Wen, F. Zhang, Y. Luo, Q. Lin, H. Zhang, X. Guo, Y. Huang, K. Nan, S. Jia, A. W. Oraham, M. B. Mevis, J. Lim, X. Guo, M. Gao, W. Ryu, K. J. Yu, B. G. Nicolau, A. Petronico, S. S. Rubakhin, J. Lou, P. M. Ajayan, K. Thornton, G. Popescu, D. Fang, J. V. Sweedler, P. V. Braun, H. Zhang, R. G. Nuzzo, Y. Huang, Y. Zhang, J. A. Rogers, Three-dimensional mesostructures as high-temperature growth templates, electronic cellular scaffolds, and self-propelled microrobots. *Proc. Natl. Acad. Sci. U.S.A.* **114**, E9455–E9464 (2017).
36. T. Ji, A. Pachi, Frequency and velocity of people walking. *Struct. Eng.* **83**, 36–40 (2005).
37. A. V. Rowlands, M. R. Stone, R. G. Eston, Influence of speed and step frequency during walking and running on motion sensor output. *Med. Sci. Sports Exerc.* **39**, 716–727 (2007).
38. P.-F. Su, S. A. Gard, R. D. Lipschutz, T. A. Kuiken, Differences in gait characteristics between persons with bilateral transtibial amputations, due to peripheral vascular disease and trauma, and able-bodied ambulators. *Arch. Phys. Med. Rehabil.* **89**, 1386–1394 (2008).

**Acknowledgments:** We thank the staff of the NUFAB, MatCI, and NUANCE facilities at Northwestern University for assistance in this research. We thank R. Stine for assistance with use of the Pliance system. **Funding:** This work was supported by the Eunice Kennedy Shriver National Institute of Child Health and Human Development (NICHD), the National Institute of Biomedical Imaging and Bioengineering (NIBIB) under grant R01EB019337, and NIH National Institute on Aging (NIA) Small Business Innovation Research Grants (SBIR) (grant no. 1R43AG059445-01). Y.H. acknowledges support from NSF (grant no. CMMI1635443). Z.X. acknowledges the support from the National Natural Science Foundation of China (grant no. 12072057) and Fundamental Research Funds for the Central Universities [grant no. DUT20RC(3)032]. X.C. acknowledges support from the National Key R&D Program of China (grant 2018YFA0108100) and China Scholarship Council. R.A. acknowledges support from the National Science Foundation Graduate Research Fellowship (NSF DGE-1842165) and Ford Foundation Predoctoral Fellowship. S.M. and C. Liu acknowledge support from the National Science Foundation Graduate Research Fellowship (NSF DGE-1842165). This work made use of the NUFAB facility of Northwestern University's NUANCE Center, which has received support from the SHyNE Resource (NSF ECCS-2025633), the IIN, and Northwestern's MRSEC program (NSF DMR-1720139). This work made use of the MatCI Facility at Northwestern University, which receives support from the MRSEC Program (NSF DMR-1720139) of the Materials Research Center at Northwestern University. **Author contributions:** J.W.K., M.H., Z.X., H.U.C., A.B., S.X., S.F., and J.A.R. developed the overall research ideas and goals. J.W.K., M.H., Z.X., H.U.C., J.Y.L., R.A., X.C., C. Liang, I.J., J.K., M.N., K.K., S.M., C. Liu, D.S.Y., and Y.P. were responsible for engineering investigations. J.W.K., M.H., X.C., C. Liang, I.J., J.K., and M.N. manufactured the sensors and devices. Z.X., R.A., X.G., and Y.H. performed the structural design and mechanical and electrical modeling. H.U.C., J.Y.L., K.K., C.O., D.G., D.R., D.H.K., and S.M. designed software for the platform. J.W.K., M.H., M.P., C. Liu, D.S.Y., and Y.P. performed in vitro characterizations. R.C. recruited participants and fabricated prostheses. J.W.K., J.Y., S.F., and R.C. performed clinical data collection and analysis. J.W.K., M.H., Z.X., R.A., J.Y., R.C., Y.H., S.F., and J.A.R. wrote the manuscript. **Competing interests:** The authors declare that they have no competing interests. **Data and materials availability:** All data associated with this study are present in the paper or the Supplementary Materials.

Submitted 24 April 2020

Accepted 17 November 2020

Published 16 December 2020

10.1126/scitranslmed.abc4327

**Citation:** J. W. Kwak, M. Han, Z. Xie, H. U. Chung, J. Y. Lee, R. Avila, J. Yohay, X. Chen, C. Liang, M. Patel, I. Jung, J. Kim, M. Namkoong, K. Kwon, X. Guo, C. Ogle, D. Grande, D. Ryu, D. H. Kim, S. Madhupathy, C. Liu, D. S. Yang, Y. Park, R. Caldwell, A. Banks, S. Xu, Y. Huang, S. Fatone, J. A. Rogers, Wireless sensors for continuous, multimodal measurements at the skin interface with lower limb prostheses. *Sci. Transl. Med.* **12**, eabc4327 (2020).

## Wireless sensors for continuous, multimodal measurements at the skin interface with lower limb prostheses

Jean Won Kwak, Mengdi Han, Zhaoqian Xie, Ha Uk Chung, Jong Yoon Lee, Raudel Avila, Jessica Yohay, Xuexian Chen, Cunman Liang, Manish Patel, Inhwa Jung, Jongwon Kim, Myeong Namkoong, Kyeongha Kwon, Xu Guo, Christopher Ogle, Dominic Grande, Dennis Ryu, Dong Hyun Kim, Surabhi Madhvapathy, Claire Liu, Da Som Yang, Yoonseok Park, Ryan Caldwell, Anthony Banks, Shuai Xu, Yonggang Huang, Stefania Fatone and John A. Rogers

*Sci Transl Med* 12, eabc4327.  
DOI: 10.1126/scitranslmed.abc4327

### Form, fit, and function

Improper fit between the prosthetic socket and the residual limb of persons with amputation causes discomfort, pressure ulcers, and altered load bearing. Kwak and colleagues developed pressure and temperature sensors to monitor the interface between a prosthesis and residual limb. The soft sensors communicated wirelessly with portable electronic devices during walking, sitting, and standing in non-amputees wearing prosthesis simulators and in two individuals with transtibial and transfemoral amputation, respectively. Results support use of wireless sensors to monitor the skin-prosthesis interface.

#### ARTICLE TOOLS

<http://stm.sciencemag.org/content/12/574/eabc4327>

#### SUPPLEMENTARY MATERIALS

<http://stm.sciencemag.org/content/suppl/2020/12/14/12.574.eabc4327.DC1>

#### RELATED CONTENT

<http://stm.sciencemag.org/content/scitransmed/10/435/eaan4950.full>  
<http://stm.sciencemag.org/content/scitransmed/11/503/eaaw5858.full>  
<http://stm.sciencemag.org/content/scitransmed/11/512/eaav8939.full>

#### REFERENCES

This article cites 37 articles, 5 of which you can access for free  
<http://stm.sciencemag.org/content/12/574/eabc4327#BIBL>

#### PERMISSIONS

<http://www.sciencemag.org/help/reprints-and-permissions>

Use of this article is subject to the [Terms of Service](#)

*Science Translational Medicine* (ISSN 1946-6242) is published by the American Association for the Advancement of Science, 1200 New York Avenue NW, Washington, DC 20005. The title *Science Translational Medicine* is a registered trademark of AAAS.

Copyright © 2020 The Authors, some rights reserved; exclusive licensee American Association for the Advancement of Science. No claim to original U.S. Government Works